nature communications

Article

https://doi.org/10.1038/s41467-025-57673-1

Activatable second-near-infrared-window multimodal luminogens with aggregation-induced-emission and aggregation-caused-quenching properties for step-imaging guided tumor therapy

Received: 25 May 2024

Accepted: 27 February 2025

Wenxiu Li, Sixin Ai, Huayong Zhu & Weiying Lin

Traditional organic luminogens, such as aggregation-caused quenching or aggregation-induced emission luminogens, only suitable to exhibit bright luminescence in the single state (i.e., solution or aggregated state), restricting their applications in heterogeneous environments. Herein, we propose a class of luminogens, aggregation-caused quenching / aggregation-induced emission dual property multimodal luminogens, which can simultaneously balance radiative and non-radiative decay processes in both the solution and aggregation states, bridging the gap between aggregation-caused quenching and aggregation-induced emission luminogens. By manipulating the rigidity planes and twisted groups of the molecules, we successfully develop a series of dual-property multimodal dyes **DPM-HD1-3** with excellent second near-infrared window (NIR-II) fluorescent, photoacoustic, and photothermal properties signals. Based on the dual-property multimodal characteristics of **DPM-HD3**, we construct a CO-activated multimodal luminogen, **DPM-HD3-CO**, for the step-imaging guided therapy in the tumor-bearing mice. **DPM-HD3-CO** can overcome the interference of tumor heterogeneity, and reveal the relationship between CO levels and treatment response in the different treatment steps via multimodal imaging. We expect that the introduction of the concept of dual-property multimodal luminogens would open up a innovative avenue for dye chemistry, offering greater possibilities for future widespread applications in the areas such as chemistry, biomedical imaging, and energy.

Organic luminescent materials have extensive applications in biomedical imaging, chemical sensors, organic light-emitting diodes (OLEDs), and optoelectronic devices[1–4] Nevertheless, practical implementation is still hindered by various limitations. Conventional organic luminogens usually emit light solely in diluted solutions but often experience aggregation-induced quenching (ACQ) in the aggregated/solid state[5–7]. In contrast, aggregation-induced emission luminogens (**AIEgens**) typically exhibit strong emission in the aggregated/solid states but weak fluorescence in diluted solutions[8,9]. These mean that the **ACQgens** and **AIEgens** are only suitable for efficient luminescence

Institute of Optical Materials and Chemical Biology, Guangxi Key Laboratory of Electrochemical Energy Materials, School of Chemistry and Chemical Engineering, Guangxi University, Nanning, Guangxi 530004, PR China. e-mail: Weiyinglin2013@163.com

in a single state (solution or solid)[10–13], thus limiting their applications in complex or heterogeneous environments.

Heterogeneity occurs at the subcellular, cellular, and organismal levels, due to genetic and phenotypic differences[14,15]. The biological systems heavily relies on the internal microenvironment (pH, viscosity, polarity, etc.) and bioactive species (reactive oxygen species, reactive sulfur species, metal ions, etc.) to maintain normal physiological processes[16,17]. Abnormal changes in the microenvironment and bioactive molecules can affect the homeostasis of biological systems, leading to the occurrence and progression of diseases[18–21]. Therefore, unraveling biological heterogeneity is of great significance for studying fundamental biology and human diseases. In this respect, biomedical imaging technology plays a crucial role in deciphering biological phenomena, structures, and mechanisms across various spatial scales and has found widespread application in disease theranostics and biological research[22–28]. Cancer is typically heterogeneous, and its environment and molecular fingerprints change over time[29,30], making precise detection and management particularly challenging. Ideal imaging-guided of cancer treatment requires for multiple imaging approaches at different stages of treatment to obtain accurate cancer heterogeneous detection and treatment response, and immediate customization of individualized treatment strategies. Nevertheless, most existing multi-modal luminescent materials **ACQgens** or **AIEgens** are prone to uneven aggregation and non-uniform concentration distribution in complex environments, resulting in compromised precision and reliability of imaging outcomes. So far, the dyes with efficient multimode luminescence in solution and aggregated state are still lacking.

In this work, we introduce the innovative concept of ACQ/AIE dual-properties multimodal luminescent agents (**DPMgens**), aiming to bridge the gap between **ACQgens** and **AIEgens**. We construct a series of multimode luminescent agents, **DPM-HD1-3**, with NIR-II fluorescent (FL), photoacoustic (PA) and photothermal properties in aggregation-liquid state by regulating the rigid plane and twisted groups of molecular engineering strategy. Leveraging the unique ACQ/AIE dual-properties multimodal luminescent properties of **DPM-HD3**, we customized a CO-activated multimodal luminescence (**DPM-HD3-CO**) for the step-imaging guided therapy of cancer. **DPM-HD3-CO** can overcome the interference of cancer heterogeneous environment, providing high-fidelity multimodal diagnostic information for different treatment stages of cancer, thereby improving cancer treatment options and rendering the personalized therapy. This study demonstrates that **DPMgens** can effectively integrate the advantages of **ACQgens** and **AIEgens** into a single molecule, overcoming the heterogeneous effects and facilitating the applications of chemical dyes in heterogeneous and complex environments.

Results

Design and synthesis of multimodal luminogens with ACQ/AIE dual properties

Traditional fluorophores commonly exhibit ACQ effects, where they have strong fluorescence in dilute solutions but weak or quenched fluorescence in aggregation states, thus favoring non-radiative relaxation processes (PA and heat signals)[9] In contrast, **AIEgens** exhibit weak emission or non-emissive in dilute solutions, yet they emit intense light in the aggregated state (Fig. 1a)[8,31]. Consequently, the single-state high emission of conventional organic materials may cause uncertainty of imaging in practical applications, as the luminogens usually aggregates in varying degrees in complex environments. We envisioned that we could tailor a class of multi-modal luminescent agents (**DPMgens**) with ACQ/AIE dual-properties that can simultaneously balance the radiative and non-radiative decay processes in solution/aggregation state. This aims to bridge the gap between **ACQgens** and **AIEgens** and thus to promote high-fidelity dual-state multi-modal applications of chemical dyes in heterogeneous environments. At the molecular level, NIR fluorophores with large planar conjugated structures usually exhibit strong luminescence in solution, while fluorescence quenching occurs in the aggregated state due to strong intermolecular π-π stacking effect[5,32]. At the morphological level, the **AIEgens** with twisted rotor groups exhibit weak/non-fluorescent state (non-radiative decay) in solution, whereas in the aggregated state (morphological level), restricted molecular vibrations and rotations lead to intense fluorescence emission (Fig. 1b)[33]. Therefore, we decided to develop **DPMgens** through manipulating rigid planes and twisted groups at the molecular and morphological levels. To construct **DMPgens** with NIR-II FL, PA, and photothermal properties, the molecular design should consider the following requirements: 1) Incorporation of the large steric hindrance groups to create more space for the rigid frameworks and twisted rotors, facilitating FL performance in both solution and aggregated states. 2) Introduction of the twisted rotor groups (such as diphenylamine, triphenylamine, tetraphene, etc.) to provide appropriate intramolecular motion and promote the photothermal and photoacoustic properties in both aggregated and liquid states. 3) Enhancement of the intramolecular donor-acceptor (D-A) interactions to achieve NIR-II absorption and emission. Based on this strategy, we used the hemicyanine dye (**HD**) as the skeleton to construct the NIR-II **DPMgens** (Fig. 1c). On the one hand, expanding the conjugated skeleton of **HD** would yield a dye with a long wavelength (**ACQ-HD**). The **ACQ-HD** dye possesses a large D-A conjugated rigid structure, potentially exhibiting good fluorescence properties in solution, while being susceptible to ACQ phenomenon in the aggregated state. On the other hand, the introduction of twist groups may convert the **HD** dyes into a dye with AIE characteristics (**AIE-HD**). The **AIE-HD** would have a high fluorescence signal in the aggregated state, while in the solution state the non-radiative transition may dominate due to high intramolecular vibration or rotation (strong photothermal and PA efficiency). By manipulating molecular strategies for twisting groups and rigid planes at the molecular and morphological levels, we could design a series of dual-state multimodal dye (**DPM-HD1-3**) with NIR-II FL, PA and photothermal properties by combining the advantages of **ACQ-HD** and **AIE-HD** dyes into a single molecule. Based on **DPMgens** dual-property multimodal properties, we planned to design an activatable theranostic agent **DPM-HD3** for the step-imaging guided cancer heterogeneity precision therapy (Fig. 1d). The dual-state multi-modal probes can overcome non-uniform aggregation effects in complex tumor microenvironments, exhibiting high-fidelity dual-state multi-modal luminescent characteristics, thus providing the promising tools for accurate detection and personalized treatment of cancer.

To gain insight into the electronic and geometry structure of the molecules, density functional theory (DFT) calculations were performed with the Gaussian 09, Revision C.01 program at the B3LYP/3-31 G(d) level. The optimized ground and excited state molecular geometry of **HD, AIE-HD, ACQ-HD** and **DPM-HD1-3** were shown in Supplementary Fig. 1a and Supplementary Data 1–6. Compared to **HD**, the introduction of the rotor group enhances the molecular geometry distortion of **AIE-HD** in the S_0 and S_1 states (−22.09° and −17.14°, respectively), which may facilitate dissipating the excited-state energy from free high-frequency rotation in solution, thus may reducing emission in solution. When introducing a large conjugated structure into **ACQ-HD** molecules, the dihedral angle of the ground S_0 and S_1 state rhodamine-anthracene core framework are 14.19° and 12.36°, respectively. This relatively planar conjugated structure may promote the fluorescence emission of **ACQ-HD** in solution, while it was prone to aggregation-induced quenching in the aggregated or solid states. When introducing the twisted groups, the dihedral angle of the S_0 state rhodamine-anthraquinone core skeleton in **DPM-HD1-3** molecules gradually decreases with the addition of the twisted structures, measuring 22.34°, 16.87°, and −12.45° respectively. Furthermore, the dihedral angles of **DPM-HD1-3** in the S_1 state gradually

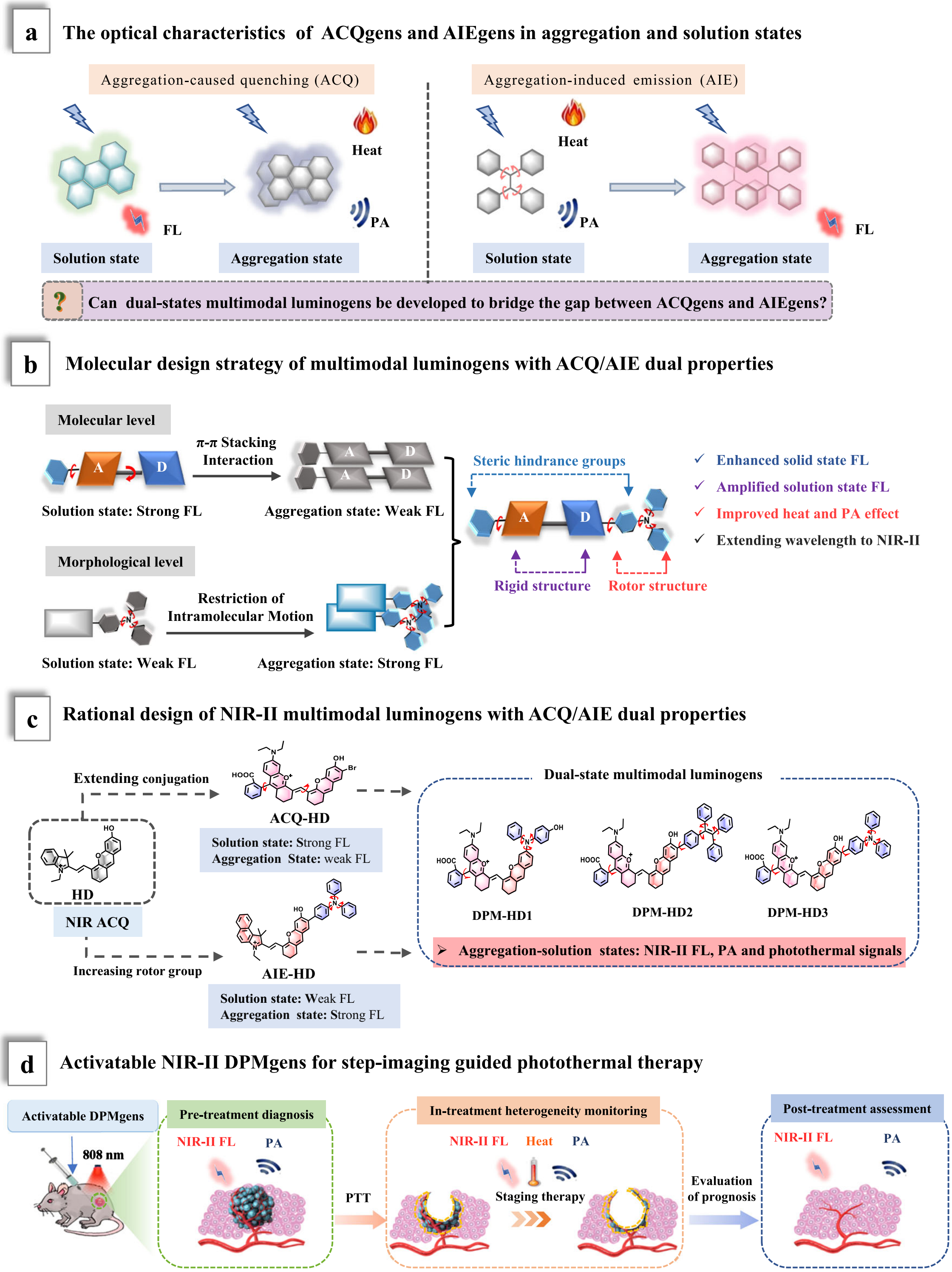

Fig. 1 | Schematic illustrations of multimodal theranostic agents with AIE/ACQ dual-properties for step-imaging guided personalized therapy. a The optical characteristics of **ACQgens** and **AIEgens** in aggregation and solution states. **b** Molecular design strategy of multimodal luminogens with AIE/ACQ dual properties. **c** Rational design of NIR-II multimodal luminogens **DPMgens** with AIE/ACQ dual properties. **d** The activatable NIR-II multimodal theranostic agents for step-imaging guided personalized photothermal therapy. **DPMgens** AIE/ACQ dual properties of multimodal luminogens, PA photoacoustic signal, FL fluorescence, PTT photothermal therapy.

approach planarity, measuring 12.89°, 0.47°, and −1.16°, which may aid the emission in solution. Notably, compared to **DPM-HD1, DPM-HD2** and **DPM-HD3** exhibit the smaller dihedral angles in the S_1 state, which may be due to the greater steric hindrance of triphenylamine (TPE) and tetraphenylethylene (TPA) compared to diphenylamine (DPA), thus promoting the formation of the molecules to adopt a relatively planar conformation.

In addition, the free rotational and vibration properties of the end rotor groups offer additional opportunities for intra-molecular motion in both the aggregated and liquid states, which can potentially coordinate the photo-thermal and photo-acoustic conversion efficiencies of the solution and aggregated states. Enhancing the electron-donating ability of the molecules can strengthen the efficient intra intramolecular charge transfer (ICT) effect of **AIE-HD** and **ACQ-HD**, reduce the energy gaps (ΔE), and favor wavelength extension (Supplementary Fig. 1b). The highest occupied molecular orbitals (HOMOs) of **DPM-HD1-3** exhibit delocalized wave functions along the diphenylamine, tetraphenylethylene, and triphenylamine units, while the lowest unoccupied molecular orbitals (LUMOs) primarily resided in the rhodamine-oxygen heterotricycles core structures. This indicated that the **DPM-HD1-3** molecules possess strong D-A characteristics and could undergo efficient intra ICT. Correspondingly, with the electron donor groups become more pronounced, the ΔE decrease gradually in the order of **DPM-HD1** (1.87 eV) > **DPM-HD2** (1.63 eV) > **DPM-HD3** (1.59 eV). This trend may facilitate their long-wavelength absorption/emission within the NIR-II biological window. Therefore, through the manipulating rigid plane and twisted structure strategy at the molecular and morphological levels, it is possible to obtain dual-state multimode luminogens with NIR-II fluorescence, photoacoustic, and photothermal properties. To achieve the **DPMgens** design objective, **ACQ-HD, AIE-HD**, and **DPM-HDs** (**DPM-HD1, DPM-HD2** and **DPM-HD3**) were synthesized following the synthetic routes described in Supplementary Figs. 2–6. The final compounds were characterized via high-resolution mass spectrum (HRMS), ^{1}H NMR, and ^{13}C NMR (Supplementary Figs. 7–33).

Photophysical property studies of DPMgens

Subsequently, we studied the photophysical properties of **AIE-HD, ACQ-HD**, and **DPM-HD1-3** in the various solvents using UV-Vis-NIR absorption spectroscopy and fluorescence spectra (Supplementary Table 1). As expected, all the dyes exhibited redshift emissions. In the solvent dichloromethane (DCM), the **AIE-HD, ACQ-HD**, and **DPM-HD1-3** exhibited maximal absorption/emission wavelengths located at 701/808, 754/915, 881/943, 813/930, and 820/932 nm, respectively (Supplementary Figs. 34–36). Notably, the absorption/emission wavelength of **DPM-HD3** in EtOH could be extended to 900/950 nm. Compared to the previously constructed NIR hemicyanine dyes **HD**, the maximal emission wavelength of **DPM-HD3** is red-shifted more than 230 nm. These results suggest that increasing the ICT effect and rigid conjugated structure can extend both absorption and emission wavelengths. To investigate the optical properties of **AIE-HD, ACQ-HD**, and **DPM-HD1-3** dyes, we examined their emission in both the solution and aggregated states. As shown in Fig. 2a, **ACQ-HD** displayed robust NIR-II FL efficiency in the dilute solution with a fluorescence quantum yields (Φ_F) of 0.404%. Conversely, the FL signal of **ACQ-HD** was obviously quenched in the solid state, possibly due to the aggregation-induced quenching effect caused by π-π stacking between molecules. In contrast, **AIE-HD** exhibited weaker fluorescence emission efficiency (Φ_F of 0.048%) in the EtOH dilute solution, whereas it shows higher fluorescence emission (915 nm) in the solid state ($\Phi_F = 0.105\%$), potentially due to the aggregation-induced emission effect. To compare the photophysical properties of **AIE-HD** and **ACQ-HD** molecules in their aggregated states, we investigated their fluorescence spectra in the various THF/H_2O (v/v) compositions. As shown in Supplementary Fig. 37a, b, when the water content (f_w) increased from 0% to 40%, the FL_{923} signal of **ACQ-HD** gradually strengthens, which may be due to the enhanced solvent polarity. However, when the f_w exceeds 40%, the FL_{923} signal decreases significantly until it reaches the baseline, possibly due to the ACQ effect and/or a reduction in solubility during aggregate formation. The FL_{815} signal of **AIE-HD** gradually intensified with increasing f_w (0–60%), which may be attributed to the AIE effect (Supplementary Fig. 37c, d). However, when f_w exceeds 70%, the FL_{815} signal gradually weakens, possibly due to molecular deposition at higher water fractions. Additionally, we further tested the absorption spectra of **ACQ-HD** and **AIE-HD** at the different water contents. The absorption of **ACQ-HD** begins to decrease when f_w exceeds 40%, while **AIE-HD** only starts to decrease when f_w exceeds 60% (Supplementary Fig. 38), indicating that their absorption reduction is also related to fluorescence quenching at high water content. At high water content (f_w = 70%), the fluorescence lifetimes of **AIE-HD** and **ACQ-HD** are 1.195 ns and 6.986 ns, respectively (Supplementary Fig. 39). The calculated acoustic loudness factor (ALF)[34] were 3.35×10^{13} and 3.04×10^{12}, respectively, (Supplementary Table 2), indicating that they have potential for photoacoustic imaging. These results indicate that **ACQ-HD** and **AIE-HD** only exhibit effective emission in a single state (dilute solution or aggregated/solid state), limiting their imaging applications in heterogeneous environments. In practice, this single-state emission characteristic increases the uncertainty of imaging, as luminescent materials typically aggregate to varying degrees in complex biological environments. Next, we examine the optical performance of **DPM-HD1-3** in the liquid and solid systems. In EtOH solution, **DPM-HD1-3** exhibited good NIR-II fluorescence emission at 908, 920, 950 nm, respectively, indicating that expanding conjugation and enhancing ICT effect contributed to lengthening the emission wavelength of the dye (Fig. 2b). In addition, compared with **AIE-HD** ($\Phi_F = 0.048\%$), **DPM-HD1-3** show higher fluorescence luminescence efficiency, with Φ_F of 0.38%, 0.25% to 0.28%. These findings suggest that the rigid conjugated backbones of **DPM-HD1-3** molecules facilitates luminescence in liquid state. The optical stability experiments (Supplementary Fig. 40) indicate that **AIE-HD, ACQ-HD**, and **DPM-HD1-3** exhibit excellent photostability, which may be favorable for long-term imaging. Notably, the **DPM-HD1-3** display strong solid-state fluorescence emissions at 1115, 1020, and 1045 nm (Fig. 2c). The **DPM-HD2** ($\Phi_F = 0.067\%$) and **DPM-HD3** ($\Phi_F = 0.072\%$) both exhibited higher solid-state FL efficiency compared to **DPM-HD1** ($\Phi_F = 0.026\%$). This may be attributed to the presence of the larger sterically hindering groups (TPE and TPA) in **DPM-HD2** and **DPM-HD3**, which may reduce face-to-face π-π stacking and thus enhance the solid-state luminescence. Furthermore, the solid-state emission of **DPM-HD1-3** showed a redshift of approximately 100 nm compared to their liquid state, likely due to the existence of the excimer. The fluorescence lifetime of **DPM-HD1-3** in the solid state were longer (2-8 times) than in the solution state (Supplementary Fig. 41 and Supplementary Table 2), further supporting the occurrence of the excimer emission in the solid state[13]. The solid-state fluorescence spectra at the different temperatures showed that **DPM-HD1-3** were not very sensitive to temperature change in the solid state. (Supplementary Fig. 42). We employed X-ray diffraction (XRD) to investigate the solid-state stacking of **DPM-HD1-3**. The **DPM-HD1-3** exhibit the strong scattering peaks at around 2θ = 25° (Supplementary Fig. 43). The interlayer distance calculated using the Bragg's equation was around 3.5 Å, suggesting that **DPM-HD1-3** have a strong π-π stacking that promotes the excimer emission in the solid state[13]. These findings illustrate that **DPM-HD1-3** demonstrate excellent NIR-II FL efficiency in both solution and solid states, which is advantageous for their imaging application in heterogeneous environments.

In addition, we further investigated the dual emission characteristics of **DPM-HD1-3** in the presence of both the solution and aggregated states. We doped an appropriate concentration (0.1 wt%) of **DPM-HD1-3** into lauric acid (LA) to construct a temperature-responsive fluorescence system (**DPM-HD1-3@LA**). LA is a natural fatty acid with a unique melting point (approximately 44 °C)[35]. As shown in Supplementary Fig. 44, when the temperature of **DPM-HD1@LA** was lowered from 60 to 30 °C, its maximum emission peak shifts from 910 to 1050 nm, resembling the fluorescence transition from the solution to solid state. **DPM-HD2@LA** and **DPM-HD3@LA** also exhibit the redshift emission from the solution to solid state. However, **HD@LA, ACQ-HD@LA** and **HD-AIE@LA** emit maximally only in the solution or solid state. This phenomenon confirms that **DPM-HD1-3** possesses the advantages of both **ACQgens** and **AIEgens**,

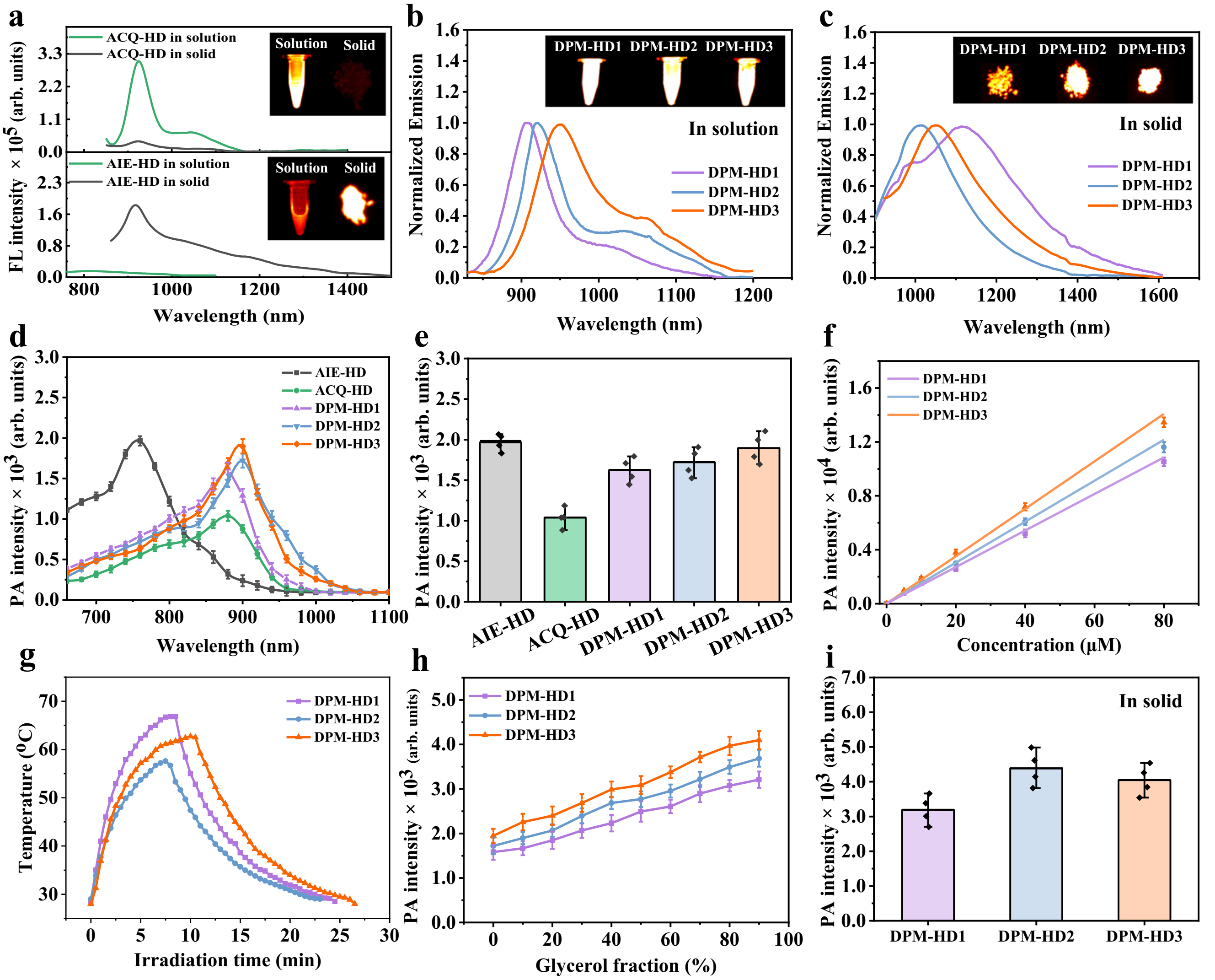

Fig. 2 | Photophysical properties of ACQ-HD, AIE-HD, and DPM-HD1-3. a FL spectra of **AIE-HD** and **ACQ-HD** in EtOH solution and solid state. The inset depicts the corresponding fluorescence images. **AIE-HD** solution λ_{ex} = 760 nm, solid state λ_{ex} = 808 nm; **ACQ-HD** solution and solid state λ_{ex} = 808 nm. **b** Normalized NIR-II FL spectra of **DPM-HD1-3** in EtOH solution. The inset shows the corresponding solution NIR-II fluorescence images. λ_{ex} = 808 nm. **c** FL spectra of **DPM-HD1-3** in solid state. The illustration is the corresponding solid state NIR-II fluorescence images. λ_{ex} = 808 nm. **d** PA spectra and **e** corresponding PA intensity of **ACQ-HD, AIE-HD**, and **DPM-HD1-3** in PBS (10 μM, pH 7.4, containing 50% EtOH). (*n* = 4 independent samples). **f** Linear relationship between PA intensity and **DPM-HD1-3** of different concentrations in EtOH solution. (*n* = 4 independent samples). **g** Photothermal heating-cooling process of **DPM-HD1-3** solutions (20 μM, pH 7.4, containing 50% EtOH) under continuous irradiation of 808 nm light (1 W cm^{-2}). **h** Relative PA intensity of **DPM-HD1-3** in DMF/glycerol mixture with different glycerol fractions. E$_x$: 880 nm. (*n* = 4 independent samples). **i** The PA strength of **DPM-HD1-3** in solid state. E$_x$: 900 nm Data are presented as the means ± s.d. (*n* = 3 independent samples). Source data are provided as a Source Data file.

enabling dual emission in both the solution and aggregated/ solid states. To understand the aggregation-state luminescence mechanism of the molecules in the aggregated state, molecular dynamics (MD) simulations of **ACQ-HD, AIE-HD**, and **DPM-HD1-3** were performed using the GROMACS program[36]. The snapshots were taken from the production simulations to illustrate the stacking modes of the molecular aggregates. As shown in Supplementary Fig. 45, the aggregates of **ACQ-HD, AIE-HD**, and **DPM-HD1-3** all exhibit disordered amorphous forms. The dimers of **ACQ-HD** display face-to-face π-π stacking, which is prone to the aggregation-induced quenching. However, due to the presence of the twisted steric groups, the dimers of **AIE-HD** and **DPM-HD1-3** exhibit the staggered π-π stacking, which is favorable for the formation of the excimer emission in the aggregated/solid state.

Next, we further investigated the PA and photothermal properties of **AIE-HD, ACQ-HD**, and **DPM-HD1-3**. First, we recorded the PA spectra of the **AIE-HD, ACQ-HD**, and **DPM-HD1-3** by measuring the PA intensity at different wavelengths. The data show good correlation between the PA spectra and absorption curves, indicating that the PA signals originate from the absorption of NIR chromophores (Fig. 2d, e). In the 50% PBS/EtOH solution, **AIE-HD** and **DPM-HD1-3** exhibit higher PA intensities than **ACQ-HD**, with the PA intensity order being **ACQ-HD** < **AIE-HD** < **DPM-HD1** < **DPM-HD2** < **DPM-HD3**. This could be due to the twisted rotor groups (such as DPA, TPE, and TPA groups) present in **AIE-HD** and **DPM-HD1-3** molecules, which may induce appropriate intramolecular motion and thereby enhancing the PA signal in solution. In addition, the PA intensity of **DPM-HD1-3** exhibits a good linear relationship with molar concentration (Fig. 2f), indicating its potential for quantitative analysis. These results indicate that **DPM-HD1-3** show excellent bimodal performance of NIR-II FL and PA in a monodispersed state. To investigate the origin of the PA signal of **ACQ-HD, AIE-HD**, and **DPM-HD1-3**, we examined their photothermal properties. Under near-infrared light irradiation, the maximum temperatures of **AIE-HD, ACQ-HD**, and **DPM-HD1-3** solution were 41.0, 49.3, 66.8, 57.6, and 62.7 °C, respectively (Fig. 2g). The photothermal conversion efficiencies (η) were 35.6, 42.2, 69.0, 58.5, and 65.3% respectively (Supplementary Figs. 46–50). It is worth noting that the photothermal conversion efficiency (PCE) of **DPM-HD3** is 23.1% higher than that of **ACQ-HD**, indicating that enhanced intramolecular motion contributes to coordinating the non-radiative transition process of the dye in the liquid state. To assess the photothermal stability of **DPM-HD1-3**, we recorded the temperature changes in the **DPM-HD1-3** solutions under continuous laser irradiation. The experimental results showed that the maximum temperature of **DPM-HD1-3** does not decrease significantly after four heating-cooling cycles under irradiation of 808 nm (1 W/ cm^2) laser (Supplementary Figs. 51–53), while the maximum of ICG (a commercial indocyanine green dye) decreased significantly (Supplementary Fig. 54). These results suggest that **DPM-HD1-3** exhibit excellent photothermal stability, which is beneficial for achieving prolonged imaging and photothermal therapy. Moreover, **DPM-HD1-3** exhibit the favorable acoustic loudness factor (ALF) in both the solution and aggregated states (Supplementary Table 2), which is advantageous for PA imaging applications in heterogeneous environments. Next, we studied the PA properties of **DPM-HD1-3** at various viscosities. As shown in Fig. 2h, the PA of the **DPM-HD1-3** molecules increases with the enhancement in glycerol content in the N, N-dimethylformamide (DMF)-glycerol mixture. In addition, their absorbance and fluorescence emission were also gradually increased with the increasing viscosity (Supplementary Figs. 55 and 56). This phenomenon may be attributed to the enhanced conjugated rigid planes of **DPM-HD1-3** under the high viscosity conditions, which increases the molar absorptivity and promotes the output of the PA and FL signal.

To verify the multimodal properties of **DPM-HD1-3** in the solid-state, we further examined the photothermal and PA performance of the solid-state **DPM-HD1-3**. The experimental findings demonstrated that the highest temperatures reached by the solid-state **DPM-HD1-3** were 95.6, 98.9, and 92.6 °C respectively, which facilitate the generation of photoacoustic signals (Supplementary Fig. 57). Next, we also investigated the PA performance of **DPM-HD1-3** in the solid state. The result demonstrate that solid state **DPM-HD1-3** still exhibits strong PA signals (Fig. 2i and Supplementary Fig. 58). These research findings demonstrate that the innovative **DPM-HD1-3** dyes can effectively regulate the radiative and non-radiative transition processes in both solid and solution states, exhibiting efficient NIR-II FL, PA, and photothermal multimode properties in solution/solid state environments. This ACQ/AIE dual-properties multimodal luminescent feature of the **DPM-HDs** chemical dyes holds great promise for applications in heterogeneous environments. Next, the size and morphology of **DPM-HD1-3** in the aggregated state were examined using dynamic light scattering (DLS) and scanning electron microscopy (SEM). As depicted in Supplementary Figs. 59–61, the hydrodynamic diameters of the **DPM-HD1-3** dyes were 108, 100, and 120 nm, respectively, with polydispersity indices (PDI) of 0.246, 0.318 and 0.226, respectively. The SEM images showed that **DPM-HD1-3** had a near-spherical morphology with an average size similar with the measurements obtained by DLS. Moreover, we assessed the pK_a values of **DPM-HD1-3** and found them to be 4.1, 7.1, and 6.7, respectively (Supplementary Figs. 62–64). This indicates that these dyes are suitable for application over a wide pH range. Overall, the **DPM-HD$_S$** can effectively balance the radiative and non-radiative transition processes in both the solid and liquid states, with unique dual-state NIR-II FL, PA, and photothermal multimodal properties, thereby potentially bridging the gaps between **ACQgens** and **AIEgens**.

Design and spectral studies of activated multimodal theranostic agents based on DPMgens

Cancer is typically heterogeneous, with its environment and molecular fingerprints changing over time, making precise detection and management particularly challenging[29,30]. Toward this end, activatable multimodal molecular theranostic agents may enable multidimensional, real-time, non-invasive assessment of oncogene-driven alterations and their therapeutic response, strengthening the effectiveness of cancer management[37–39]. However, most of the existing multimodal molecular theranostic agents rely on the use of **ACQgens** or **AIEgens** dyes, which are susceptible to heterogeneous aggregation effects in complex and variable environments, leading to false positive or negative imaging results. Therefore, the development of activated multimodal theranostic agents is of great significance for the accurate detection and personalized treatment of complex diseases. Endogenous CO, produced by the family of heme oxygenase (HOs), serves as a vital gas-signaling molecule that plays a regulatory role in various physiological processes and pathologies[40]. CO is involved in the regulation of key signaling pathways in physiological systems, exerting anti-inflammatory, anti-apoptotic and anti-proliferation effects[41,42]. It is worth noting that abnormal levels of the endogenous CO are closely associated to the development process of cancer. Thus, spatiotemporal dynamic monitoring of the relationship between CO levels and treatment response during different treatment stage is crucial for diagnosing, managing tumor heterogeneity. Leveraging the unique dual-property multimodal luminescence characteristics of **DPM-HD3**, we have constructed a CO-activated multimodal theranostic agent, **DPM-HD3-CO**, for the step-imaging guided therapy of tumor heterogeneity (Fig. 3a). The theranostic agent **DPM-HD3-CO** uses an allyl chloroformate functionalized **DPM-HD3** dye as the CO sensing moiety and $PdCl_2$ as the additive to capture CO. The sensing mechanism of **DPM-HD3-CO** relies on CO converting Pd^{2+} to Pd^0, which then triggers the Tsuji–Trost reaction to remove the allyl group[43,44]. The agent **DPM-HD3-CO** initially would not exhibit NIR-II FL/PA/PTT signals as the dye **DPM-HD3** was in the caged state. When the probe system (**DPM-HD3-CO** + $PdCl_2$) specifically responds to tumor-associated CO, **DPM-HD3** would be released, thus switching on NIR-II FL, ratio-PA, and photothermal signals for the step-imaging guide therapy of tumor heterogeneity. The NIR-II FLI enables rapid tumor site localization, while PA imaging can provide the detailed information, such as tumor 3D geometry and depth, providing clear guidance for personalized treatment. PTI can provide sensitive and rapid feedback to the phototherapy response. More importantly, **DPM-HD3-CO** can overcome the heterogeneous accumulation effect in a heterogeneous disease environment to provide high-fidelity multimodal diagnostic information. Therefore, the developed activatable multimodal theranostic agent **DPM-HD3-CO** was expected to decipher tumor information in pathological settings at the different treatment stages, timely adjust the treatment plan of tumors, and improve the precision of tumor treatment. The synthetic pathway of **DPM-HD3-CO** was depicted in Supplementary Fig. 65, and its structure was characterized using ^1H NMR, ^{13}C NMR and HRMS (Supplementary Figs. 66–68).

To investigate the feasibility of **DPM-HD3-CO** for NIR-II FL/ratio PA sensing of CO, we evaluated the optical properties and targeted recognition capabilities of the probe **DPM-HD3-CO** in vitro. First, the probe **DPM-HD3-CO** response to CO was tested in the presence of $PdCl_2$. Commercially available $[Ru(CO)_3Cl$ (glycinate)] (CORM-3, a classic CO-releasing molecule) was used as the CO donor[43,45,46]. As shown in Fig. 3b, the free **DPM-HD3-CO** exhibits a maximum absorption wavelength of 690 nm. Upon the addition of CORM-3 (0–100 μM), the absorption at 690 nm gradually decreased, while a characteristic peak corresponding to the **DPM-HD3** dye appeared at 900 nm. When the CORM-3 concentration was 100 μM, the absorbance ratio Abs_{900}/Abs_{690} increased from 0.02 to 2.39, suggesting that **DPM-HD3-CO** can be utilized for the ratiometric detection of CO, thereby enhancing the

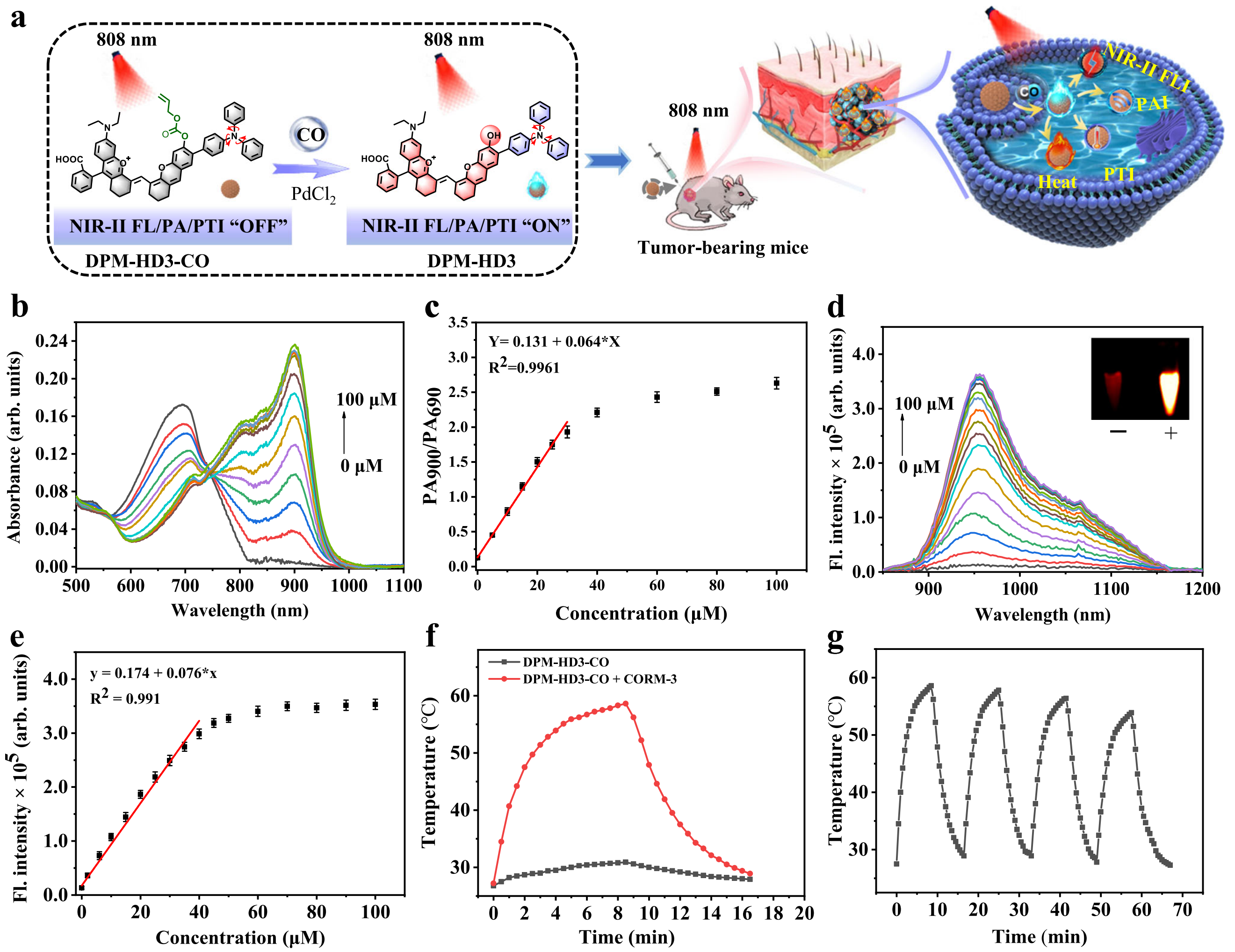

Fig. 3 | Design and spectral studies of CO-activated multimodal theranostic agent. a Schematic illustrations of CO-activated multifunctional theranostic agent (**DPM-HD3-CO**) for multimodal diagnose guided personalized therapy. **b** Absorption spectra of probe system (**DPM-HD3-CO** + $PdCl_2$, 10 μM each) after adding CORM-3 at different concentrations in PBS (10 mM, pH 7.4, containing 50% EtOH). **c** The relationship between PA_{900}/PA_{690} and CORM-3 concentration. ($n = 3$ independent samples). **d** Fluorescence spectra of probe system (**DPM-HD3-CO** + $PdCl_2$, 10 μM each) responding to CORM-3 (0–100 μM). The inset is the fluorescence imaging of the **DPM-HD3-CO** solution before and after the reaction. $\lambda_{ex} = 808$ nm. **e** The relationship between FL_{950} and CORM-3 concentration. ($n = 3$ independent samples). **f** The heating and cooling photothermal curves before and after the reaction of **DPM-HD3-CO** with CORM-3. **g** Photothermal stability of **DPM-HD3-CO** responding to CO in aqueous solution during four on/off irradiation cycles with an 808 nm laser (1 W cm^{-2}). Data are presented as the means ± s.d. Source data are provided as a Source Data file.

accuracy and reliability of the measurement. The time-dependent study found that the intensity of Abs_{900} gradually increased with prolonged time, reaching a plateau at 25 min, indicating the probe **DPM-HD3-CO** possesses the ability to detect CO rapidly (Supplementary Fig. 69). Furthermore, we also investigated the PA properties of the **DPM-HD3-CO**. The PA spectra were measured in the wavelength range of 680 to 1064 nm before and after the reaction of **DPM-HD3-CO** with CORM-3. The free **DPM-HD3-CO** displayed a strong PA signal at 690 nm (PA_{690}), while the 900 nm PA signal was very weak ($PA_{900}/PA_{690} \sim 0.11$). Upon reaction with CORM-3, the PA_{900} signal significantly increased, while the PA_{690} signal decreased, resulting in an approximately 24-fold enhancement of the PA_{900}/PA_{690} signal (Supplementary Fig. 70). A dose-dependent enhancement of the PA_{900}/PA_{690} signal was observed when **DPM-HD3-CO** was treated with different concentrations of CORM-3 (Fig. 3c and Supplementary Fig. 71). The PA_{900}/PA_{690} exhibited a good linear relationship with CORM-3 concentrations from 0–30 μM, with a detection limit of 8.2×10^{-7} M, indicating that **DPM-HD3-CO** exhibits excellent PA ratio. Additionally, the NIR-II fluorescence intensity at 950 (FL_{950}) increased by approximately 26.7-fold after incubation with various concentrations of CORM-3 (Fig. 3d) and demonstrated a positive linear relationship with CORM-3 concentration (0–40 μM), with a detection limit of 4.7×10^{-7} M (Fig. 3e). These results suggest that the probe **DPM-HD3-CO** exhibits sensitive response to CO in both NIR-II FL and PA dual-modal modes. The response mechanism of the probe to CORM-3 was verified by high-resolution mass spectrometry (HRMS) and liquid chromatography-mass spectrometry (LC-MS). The HRMS analysis revealed the presence of a distinct mass spectral peak at m/z 829.3846 after the reaction between the probe and CORM-3, corresponding to the molecular weight of the [**DPM-HD3**] dye (Supplementary Fig. 72). In addition, the LC-MS results showed that there was a major ion peak of m/z 829.3606 at the retention time of 19.17 min (Supplementary Fig. 73), which matches the expected compound **DPM-HD3** ($[M]^+$, calculated m/z 829.3636). The ion peak of m/z 913.3819 is attributed to the probe **DPM-HD3-CO** ($[M]^+$, calculated m/z 913.3847) at the retention time of 19.60 min. These results demonstrate that the probe **DPM-HD3-CO** can react with CO to release the dye **DPM-HD3** under physiological conditions, thereby activating NIR-II FL_{950} and PA_{900}/PA_{690}

signals. Next, we investigated the selectivity of **DPM-HD3-CO**. The results showed that only CO exhibited the significant Abs_{900} signal enhancement, while the absorption changes of other analytes were almost negligible (Supplementary Fig. 74a). We also further examined the chemical stability of the probe in the presence of the different concentrations of $ONOO^-$. The results showed that the **DPM-HD3-CO** structure may be partially damaged at a concentration of 100 μM $ONOO^-$ (Supplementary Fig. 74b). However, as shown in Supplementary Fig. 74c, the Abs_{900} values of the probe treated with 15 μM CORM-3 are similar in the presence or absence of 15 μM $ONOO^-$, suggesting that the probe **DPM-HD3-CO** has a selective response to CORM-3. Moreover, the pH sensitivity of **DPM-HD3-CO** was also examined. As depicted in Supplementary Fig. 75, the Abs_{900} signals of the probe exhibited negligible changes within the pH range of 3.0–9.0. However, upon the addition of CORM-3, the **DPM-HD3-CO** solution exhibited excellent responses within the physiological pH range of 6.5–8.5, indicating that the **DPM-HD3-CO** is capable of detecting CO within a wide range of physiological pH values. Furthermore, the photothermal efficacy of **DPM-HD3-CO** was assessed before and after its response to CO by monitoring the temperature variation in the probe solution upon exposure to an 808 nm laser with a power of 1 W/cm^2. As shown in Fig. 3f and Supplementary Fig. 76, the temperature of the CO-activated probe increased significantly (58.3 °C) within 8 min, whereas the free probe exhibited negligible temperature changes under the same conditions. Additionally, the results of the reversible heating-cooling experiments showed that the maximum temperature of the CO-activated probe remained nearly constant for at least four cycles, indicating the superior photothermal stability of **DPM-HD3-CO** (Fig. 3g). Taken together, these results confirm that the probe **DPM-HD3-CO** could serve not only as an activatable NIR-II FL/ratio-PA probe for CO detection but also as an efficient photothermal agent.

Assessment of imaging and photothermal therapy of activated theranostic agent in cancer cells

To investigate the response of the **DPM-HD3-CO** toward CO in cells, FL and PA imaging was performed on the hepatocellular carcinoma cells (Hepa1-6) and normal hepatocytes (HL-7702). Prior to the cell imaging, the cytotoxicity of the **DPM-HD3-CO** was evaluated using the Cell Counting Kit-8 (CCK-8) method in both Hepa1-6 and HL-7702 cell lines. After incubation with the **DPM-HD3-CO** (50 μM) for 24 h, the survival rate of both cell lines was still higher than 82% (Supplementary Fig. 77), indicating that the probe **DPM-HD3-CO** had low toxicity for both the normal and cancer cells. Subsequently, the ability of the probe **DPM-HD3-CO** to image CO in cells was investigated. The previous studies have indicated that cancer cells release more endogenous CO than normal cells[47]. As shown in Supplementary Fig. 78, the signal intensity of FL_{950} and ratio PA_{900}/PA_{690} in Hepa1-6 cells was significantly higher than that in HL-7702 cells, indicating that the levels of CO in the cancer cells may be higher than the normal cells. Additionally, after pretreating Hepa1-6 cells with zinc protoporphyrin (ZnPP, a typical endogenous CO scavenger) for 1 h, the FL_{950} and ratio PA_{900}/PA_{690} signals decreased significantly. These results further indicate that **DPM-HD3-CO** can selectively recognize the increased CO level in the cancer cells, thereby activating FL and PA dual-modal signals. To further validate that **DPM-HD3-CO** can effectively identify CO levels in cancer cells, we used a commercial CO probe system, 3′, 6′-Bis (allyloxy)-Fluoran, for confocal imaging of the cells (Supplementary Fig. 79). The results showed that the green fluorescence signal of Hepa1-6 cancer cells was significantly higher than that of HL-7702 normal cells. The imaging results from the commercial CO probe were consistent with those from **DPM-HD3-CO**, further confirming that **DPM-HD3-CO** can detect the increased endogenous CO level in the cancer cells. To investigate the PTT effect of **DPM-HD3-CO** on HL-7702 and Hepa1-6 cells, we used a dual-staining method with Calcein-AM (staining live cells, green fluorescence) and propidium iodide (PI, staining dead cells, red fluorescence) to evaluate the phototoxicity of **DPM-HD3-CO** (Supplementary Fig. 79). As expected, significant green fluorescence was observed in the cells treated with PBS or PBS + laser, indicating low phototoxicity of the utilized laser. Meanwhile, the cells cultured with **DPM-HD3-CO** without laser irradiation also showed significant green fluorescence, further suggesting low toxicity of **DPM-HD3-CO** to both the cancer cells and normal cells. In contrast, when the cells were treated with **DPM-HD3-CO** + laser, significant red fluorescence was observed in Hepa1-6 cells, while the HL-7702 cells exhibited green fluorescence, indicating that the probe can selectively kill the cancer cells. The viability of the cells was further assessed by the MTT assay. The data in Supplementary Fig. 80 showed that the viability of HL-7702 and Hepa1-6 cells was still 82% after PBS + Laser or the probe treatment, indicating that only the laser irradiation or probe treatment is less toxic to the normal or cancer cells. The results of the results of Probe + Laser treatment demonstrated that the viability of HL-7702 cells was still higher than 80%, while the viability of Hepa1-6 cells was about 10%, indicating that the probe had targeted photothermal therapeutic effect on the cancer cells. These results suggest that **DPM-HD3-CO** can serve as a CO-activated therapeutic diagnostic agent for in-situ photothermal therapy of cancer cells, with minimal side effects.

In vivo multimodal imaging using activated theranostic agent

Next, to evaluate the in vivo NIR-II FL imaging performance, **DPM-HD3-CO** was injected separately into the normal muscle tissue and tumor of the thighs of the mice, and then recorded and analyzed their NIR-II FL_{950} signal. Prior to the administration of **DPM-HD3-CO**, no significant FL_{950} signal was observed in the normal muscle tissue and tumor in the thighs of the mice (Fig. 4a). After 0.5 h of injecting the **DPM-HD3-CO**, the FL_{950} intensity in the tumor site was significantly higher (4.2 times) than that in the normal muscle tissue (Fig. 4b). This indicates that the level of CO in the tumor is higher than that in the normal muscle tissue, and that the abundance of CO in the tumor microenvironment can activate the fluorescence signal of the **DPM-HD3-CO**. Over the course of time, there was a gradual decrease in the NIR-II FL signal at the tumor, likely due to the metabolism of the activated probe within the mouse. Remarkably, even after 48 h, the significant NIR-II FL signal continued to be observed at the tumor site, suggesting the **DPM-HD3-CO** tremendous potential for monitoring and tracking tumor development over an extended period. Additionally, we conducted the 3D ratio PA imaging of the tumors. As shown in Fig. 4c, d, a strong PA_{690} signal and a weak PA_{900} signal were observed at the tumor site following probe injection (0 h), with a PA_{900}/PA_{690} ratio of 0.34. As time progressed, the PA_{690} signal gradually decreased while the PA_{900} signal gradually increased, and the PA_{900}/PA_{690} ratio increased about 4.2-fold at 0.5 h. Over time, the signal intensity of PA_{900}/PA_{690} decreased to about 0.89, which may be due to the metabolism, clearance or different properties upon cellular uptake of the probe in the heterogeneous tissues. Notably, due to its good retention ability in the tumor tissue, the signal was still clearly identifiable even after 48 h. In addition, the 3D PA imaging depth analysis showed that the imaging depth of the **DPM-HD3-CO** was about 10 mm (Supplementary Fig. 81), indicating that the probe had a good tissue penetration depth. These results suggest that that the probe could depict the spatial profile of deep tumor tissues through 3D PA imaging, providing deep non-invasive anatomical information for the detection of cancer. By taking full advantage of the high sensitivity of FL technology, and the good penetration ability and spatial resolution of PA imaging, **DPM-HD3-CO** could provide comprehensive diagnostic information for cancer, which is beneficial to guide doctors to customize personalized treatment plans. Next, we investigated the photothermal imaging performance of the probe **DPM-HD3-CO** in the tumor-bearing mice. As shown in Fig. 4e, the photothermal signal of the probe + laser group exhibited gradual increased with the

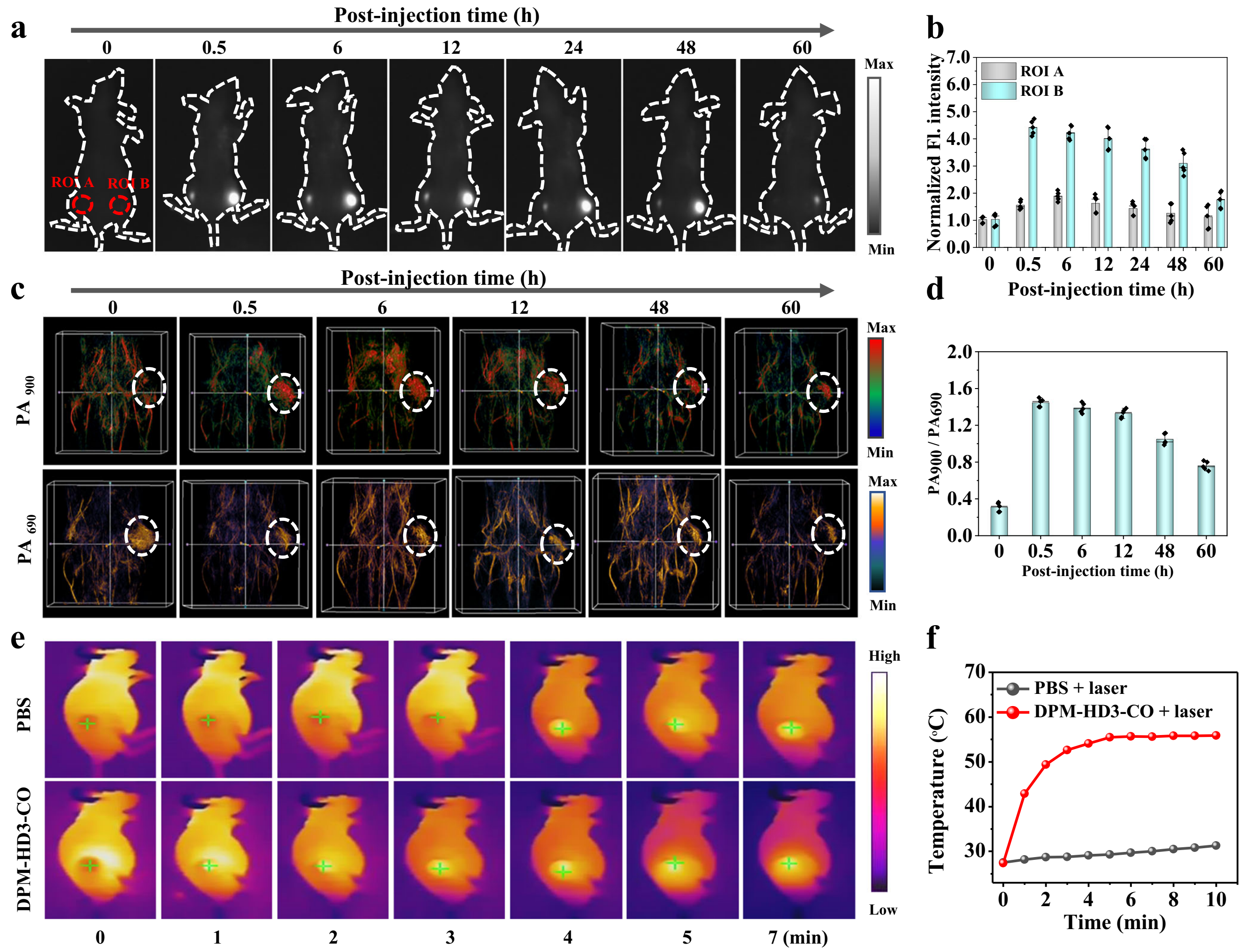

Fig. 4 | In vivo multimodal imaging using activated theranostic agent. a The representative NIR-II FL imaging of the normal muscle tissue (ROI A) and tumor (ROI B) in the thighs of the mice at different times points (0, 0.5, 6, 12, 48 and 60 h) after intratumoral injection of 20 μM **DPM-HD3-CO** (100 μL, including 10 μM $PdCl_2$). Imaging parameters: 808 nm laser, 880 nm long-pass filters. **b** Corresponding mean intensity of NIR-II FL imaging. ($n = 5$ mice). **c** PA imaging of tumor regions at different times points (0, 0.5, 6, 12, 48 and 60 h) after intratumoral injection of 20 μM **DPM-HD3-CO** (100 μL, including 10 μM $PdCl_2$). The meaning of the colors were indicated in the color bars: The red and green represent PA_{900} channel. The orange and purple represent PA_{690} channel. **d** Corresponding mean intensity of the PA imaging. ($n = 5$ mice). **e** PTI of the tumor exposed to continuous laser irradiation (808 nm, 1 W cm^{-2}, 0–7 min) after post-injection of PBS and 20 μM **DPM-HD3-CO** (100 μL, including 10 μM $PdCl_2$). ($n = 5$ mice). The yellow represent PTI channels. Imaging effects of NIR-II FLI, PAI, and PTI before and after photothermal treatment (Laser: 808 nm, 1 W cm^{-2}). **f** The corresponding temperature intensity in (**e**). The excitation source is an 808 nm laser and FLI was collected by 880 nm long-pass filter with an exposure time of 100 ms. Data are presented as the means ± s.d. ($n = 5$ mice). Source data are provided as a Source Data file.

illumination time, reaching 55.9 °C within five minutes (Fig. 4f). Moreover, the temperature at the tumor site only showed a slight increase in the PBS + laser group after 6 min of irradiation. The above results show that the increased CO level within the tumors can activate the photothermal properties of **DPM-HD3-CO**, thus reducing the photothermal damage to the normal tissues and realizing the effect of activating the photothermal therapy in situ. Furthermore, fluorescence imaging of metabolism and major organs in vivo show that the probe could respond at the tumor site and can be metabolically cleared through the liver in vivo (Supplementary Figs. 82 and 83). These results suggest that the activated probe **DPM-HD3-CO** can perform NIR-II FL, PA, and photothermal tri-modal imaging of increased endogenous CO level within the tumors, with the potential for long-term companion diagnostics in vivo.

Tracking the heterogeneous distribution of theranostic agent in cancer cells and tumor tissue

In order to investigate the distribution of theranostic agent **DPM-HD3-CO** in complex cancer cells and tumors tissue microenvironment, we conducted confocal image on cancer cells and tumors tissue with different treatments (Fig. 5a). First, to investigate the distribution of the probe **DPM-HD3-CO** in Hepa1-6 cells under the different treatments, **DPM-HD3-CO** (20 μM) was incubated with Hepa1-6 cells for 30 min, followed by the laser treatment. Then, the laser confocal microscopy was used to image the Hepa1-6 cells, and the aggregate size was measured using the Nano Measurer software. As shown in Fig. 5b and Supplementary Fig. 84, compared to the PBS group, **DPM-HD3-CO** was distributed in the aggregated state within the cancer cells with the aggregate sizes mainly at 600 nm. However, upon the 808 nm laser irradiation, the aggregate size of **DPM-HD3-CO** reduced to approximately 300 nm. These findings indicate that the alterations in the cancer cell microenvironment are likely to affect the heterogeneous distribution of **DPM-HD3-CO**. Next, we further examined the possible impact of the probe **DPM-HD3-CO** heterogeneous distribution on imaging performance (Fig. 5c). The Hepa1-6 cells treated with PBS, probe, or probe + laser were digested with trypsin and centrifuged to obtain the cell pellets for FL and PA imaging. The results show that probe **DPM-HD3-CO** treatment group exhibited prominent

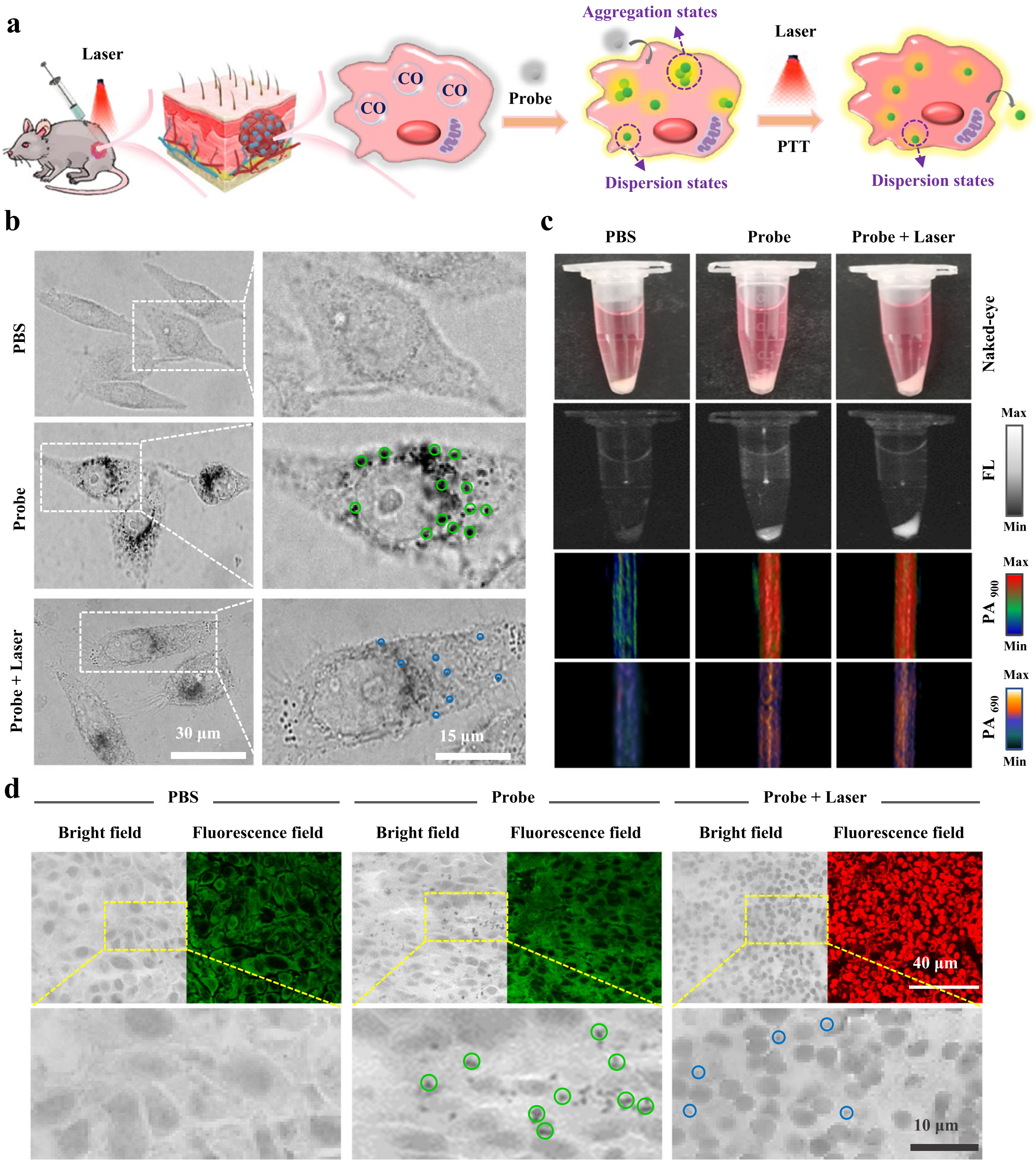

Fig. 5 | Distribution of the theranostic agent DPM-HD3-CO in the Hepa1-6 cells and tumor tissue microenvironment. a Illustration of the heterogeneous distribution of the **DPM-HD3-CO** in tumor tissue at different treatment stages following intratumoral injection of **DPM-HD3-CO**. **b** Representative confocal bright field images of Hepa1-6 cells treated with PBS, only probe system (20 μM **DPM-HD3-CO** + 10 μM $PdCl_2$), and probe system (20 μM **DPM-HD3-CO** + 10 μM $PdCl_2$) with laser irradiation (808 nm). Each experiment was repeated independently 5 times ($n = 5$), and similar results were obtained. Green circles show the aggregates of the probe **DPM-HD3-CO**, and the blue circles indicate the smaller aggregates of the **DPM-HD3-CO**. **c** Representative naked-eye, NIR-II FL and PA images of the Hepa1-6 cell pellets treated with PBS, probe system (20 μM **DPM-HD3-CO** + 10 μM $PdCl_2$), probe system (20 μM **DPM-HD3-CO** + 10 μM $PdCl_2$) + laser. The meaning of the colors were indicated in the color bars: The gray and white represent FL channels. The red and green represent PA_{900} channel. The orange and purple represent PA_{690} channel. FL imaging parameters: λ_{ex}: 808 nm, 880 nm long-pass filters. PA_{900} images excitation wavelength: 900 nm. PA_{690} images excitation wavelength: 690 nm. Each experiment was repeated independently 5 times ($n = 5$), and similar results were obtained. **d** Representative confocal bright field images and live/dead cell staining fluorescence images of the tumor tissue sections from the PBS, probe system (20 μM **DPM-HD3-CO** + 10 μM $PdCl_2$), probe system (20 μM **DPM-HD3-CO** + 10 μM $PdCl_2$) + laser groups. Each experiment was repeated independently 5 times ($n = 5$ mice), and similar results were obtained. Green fluorescence indicates the signal from Calcein-AM staining (λ_{ex}: 490 nm); representing living cells, while red fluorescence indicates propidium iodide staining (λ_{ex}: 535 nm); represents dead cells. Green circles show the bigger aggregates of the probe **DPM-HD3-CO**, and the blue circles indicate the smaller aggregates of the probe **DPM-HD3-CO** + laser. Data were expressed as mean ± SD. Source data are provided as a Source Data file.

FL and PA signals, indicating that the probe has good dual-mode emission in the aggregation state. Furthermore, after probe + laser treatment, the cells still exhibited bright NIR-II FL/PA dual-modal signals (Supplementary Fig. 85). These indicate that the FL and PA signals of the probe were not easily affected by changes in the aggregation state. Next, we further compared the imaging performance of **DPM-HD3-CO** with **AIE-HD** and **ACQ-HD** in the Hepa1-6 cells (Supplementary Fig. 86). **AIE-HD** showed aggregated distribution in the cells and exhibited stronger FL signals in the cell pellets, while **AIE-HD** + Laser exhibited smaller aggregates in the cells and showed stronger PA signals in the cell pellets. **ACQ-HD** showed aggregated distribution in the cells and exhibited stronger PA signals in the cell pellets, while

ACQ-HD + Laser exhibited smaller aggregates in the cells and showed stronger FL signals in the cell pellets. These observations suggest that the FL/PA signal outputs of **AIE-HD** and **ACQ-HD** are sensitive to the changes in the aggregate sizes, which may affect the accuracy of the imaging. In comparison, the **DPM-HD3-CO** treatment group exhibited aggregated distribution in Hepa1-6 cells and showed strong FL/PA dual-mode signals in the cell pellets, while the **DPM-HD3-CO** + Laser group showed smaller aggregates in the cells and still displayed the stable FL and PA dual-mode signals in the cell pellets, indicating that **DPM-HD3-CO** can overcome the impact of heterogeneous distribution on imaging performance. Next, we also further compared the imaging performance of **DPM-HD3-CO** with **AIE-HD** and **ACQ-HD** in the tumor tissue sections (Supplementary Fig. 87). **AIE-HD, ACQ-HD**, or **DPM-HD3-CO** (each 20 μM, 100 μL) were intratumorally injected into the tumors, respectively, followed by laser exposure. **AIE-HD** showed aggregated distribution in the tumor tissue section and exhibit stronger FL signals in the tumor, while **AIE-HD** + Laser exhibited smaller aggregates in the tumor tissue section and showed stronger PA signals in the tumor. **ACQ-HD** showed aggregated distribution in the tumor tissue section and exhibited stronger PA signals in the tumor, while **ACQ-HD** + Laser exhibited smaller aggregates in the tumor tissue section and showed stronger FL signals in the tumor. The FL and PA signal outputs of **AIE-HD** and **ACQ-HD** were susceptible to the changes in the aggregation state, which was consistent with the observations in the Hepa1-6 cells. In contrast, the **DPM-HD3-CO** treatment group exhibited aggregated distribution in the tumor tissue section and showed strong FL/PA dual-mode signals in the tumor, while the **DPM-HD3-CO** + Laser group showed smaller aggregates in the tumor tissue section and still exhibited the stable FL and PA dual-mode signals in the tumor. These results further suggest that **DPM-HD3-CO** can overcome the impact of heterogeneity distribution on imaging performance in the tumor tissues, improving the accuracy of cancer detection and treatment evaluation. To assess the impact of the heterogeneous distribution on therapeutic efficacy, we conducted the tests on the photothermal performance of **DPM-HD3-CO** under various tumor tissue microenvironments (Fig. 5d). Compared to the PBS control group, the probe-treated group showed a predominant aggregated distribution within the intercellular spaces of the tumor tissue (size approximately 600 nm), accompanied by a noticeable green fluorescent signal. In contrast, the probe + laser-treated group exhibited the smaller aggregates (size around 300 nm) but had intense red fluorescence signals. These results indicate that the probe's heterogeneous distribution does not affect its photothermal therapeutic efficacy in the different pathological environments. Therefore, based on its unique dual-property multimodal properties, the agent **DPM-HD3-CO** can overcome the influence of heterogeneous distribution on FL, PA, and PTT performance, helping improve the accuracy of disease detection and treatment in complex physiological/pathological environments.

Activatable multimodal theranostic agents for step-imaging guide personalized photothermal therapy

Cancer is a complex and heterogeneous disease characterized by intricate interactions among different tumor cells and their changing microenvironment[48]. This heterogeneity results in each type of cancer, and even each group of cancer cells, being unique in its characteristics. Hence, it is imperative to consider this aspect during cancer treatment and devise "personalized" treatment plans tailored to individual patients. To address this challenge, we have proposed a step-imaging guided therapy approach that can monitor the treatment response of patients at different stages by detecting specific biomarkers, thus enabling the development of personalized treatment plans for different patients. Based on its unique dual-property multimodal characteristics, the agent **DPM-HD3-CO** can overcome the influence of heterogeneous aggregation, and provide highly accurate diagnostic information for different stages of cancer treatment. We investigated the phototherapy effect of the theranostic agent **DPM-HD3-CO** for the cancer step-imaging guided therapy (Fig. 6a). The Hepa1-6 tumor-bearing nude mice were randomly divided into four groups: PBS, PBS + laser, **DPM-HD3-CO**, and **DPM-HD3-CO** + laser groups. Given the heterogeneity within the tumor, multimodal imaging of the treatment group mice is necessary at different stage of treatment to guide precise photothermal therapy. In clinical practice, the most challenging problem in the process of tumor treatment is to judge whether there are residual tiny tumors after treatment of large tumors and accurately decipher the spatial distribution of tiny tumors. The integration of NIR-II FL and PA imaging has comprehensive advantages such as excellent sensitivity, high spatial resolution, and deep imaging depth, making it an ideal diagnostic method in cancer treatment. During the pre-treatment stage, the probe **DPM-HD3-CO** (20 μM, 100 μL) was intratumorally injected into the tumor, followed by NIR-II FL, PA, and PT imaging. The experimental results showed the enhanced NIR-II FL (5.89 times), PA_{900}/PA_{690} (5.31 times), and PT signals at the tumor site of the Hepa1-6 tumor-bearing mice compared to the muscle tissue in the thighs of the normal mice (control group) (Fig. 6b, Supplementary Fig. 88). Diagnostic information such as tumor location, depth, and spatial distribution at the pre-treatment stage could be obtained based on activated 3D PA signals (Supplementary Movie 1). At the same time, the response of the tumor mice to photothermal therapy was evaluated through thermographic imaging. In the first-step treatment, the mice were treated with intratumoral injection of 100 μL **DPM-HD3-CO** (20 μM) and then subjected to segmented irradiation at the tumor site (808 nm, 1 W/cm^2) for 6 min each time, repeated 4 times with a 20-min interval between each treatment. On the 9th day after the completion of the first-step treatment, NIR-II FL, PA_{900}/PA_{690}, and PT imaging were performed to assess the therapeutic effect and prognosis of the tumor. After the first-step of the treatment, there should be no significant enhancement of FL and PA_{900}/PA_{690} signals at the treatment site if the tumor has been completely eradicated. However, NIR-II FL, PA_{900}/PA_{690}, and PT signals were still observed in the mice, indicating the residual tiny tumors in their bodies. At this point, 3D PA imaging could be used to observe the spatial position and depth of residual tumors at the microscopic spatial scale (Supplementary Movie 1), guiding further treatment. In addition, we conducted the ex vivo and hematoxylin and eosin (H&E) analysis of the tumors in the pre-treatment and the first-step treatment groups. The experimental results showed that, the first-step treatment group still had the residual tumors, compared to the pre-treatment group (Supplementary Fig. 89). After confirming the presence of the residual tumor, the second-step PTT treatment was conducted to eradicate the residual tumor. The **DPM-HD3-CO** (20 μM, 100 μL, including 10 μM $PdCl_2$) were intratumorally injected directly into the area of the residual tumor, followed by fractional irradiation of the tumor site with an 808 nm laser, three times per session, repeated twice with a 10-min interval between each session. After the completion of the second-step PTT treatment, the NIR-II FL, PA_{900}/PA_{690}, and PT signal intensities in the Hepa1-6 tumor-bearing mice were nearly identical to those in the normal control group (Supplementary Fig. 90), indicating essentially complete eradication of the tumor. These results suggest that **DPM-HD3-CO** can overcome the interference of cancer heterogeneous environments, providing high-fidelity multimodal diagnostic information for the different stages of cancer treatment, thereby enhancing the accuracy of cancer treatment and achieving personalized therapy.

To examine the efficacy of the step-imaging guided therapy strategy, the survival rate study was performed for the different treated mice. As depicted in Fig. 6c, following 36 days of treatment, the survival rates of the mice in the PBS, **DPM-HD3-CO** and PBS + laser treated groups all decreased to 0%. In sharp contrast, the **DPM-HD3-CO** + laser group exhibited a high survival rate of 87.5% after 25 days of treatment. Furthermore, throughout the 50-day study period, the survival rate of the mice remained consistently at 87.5%, with no

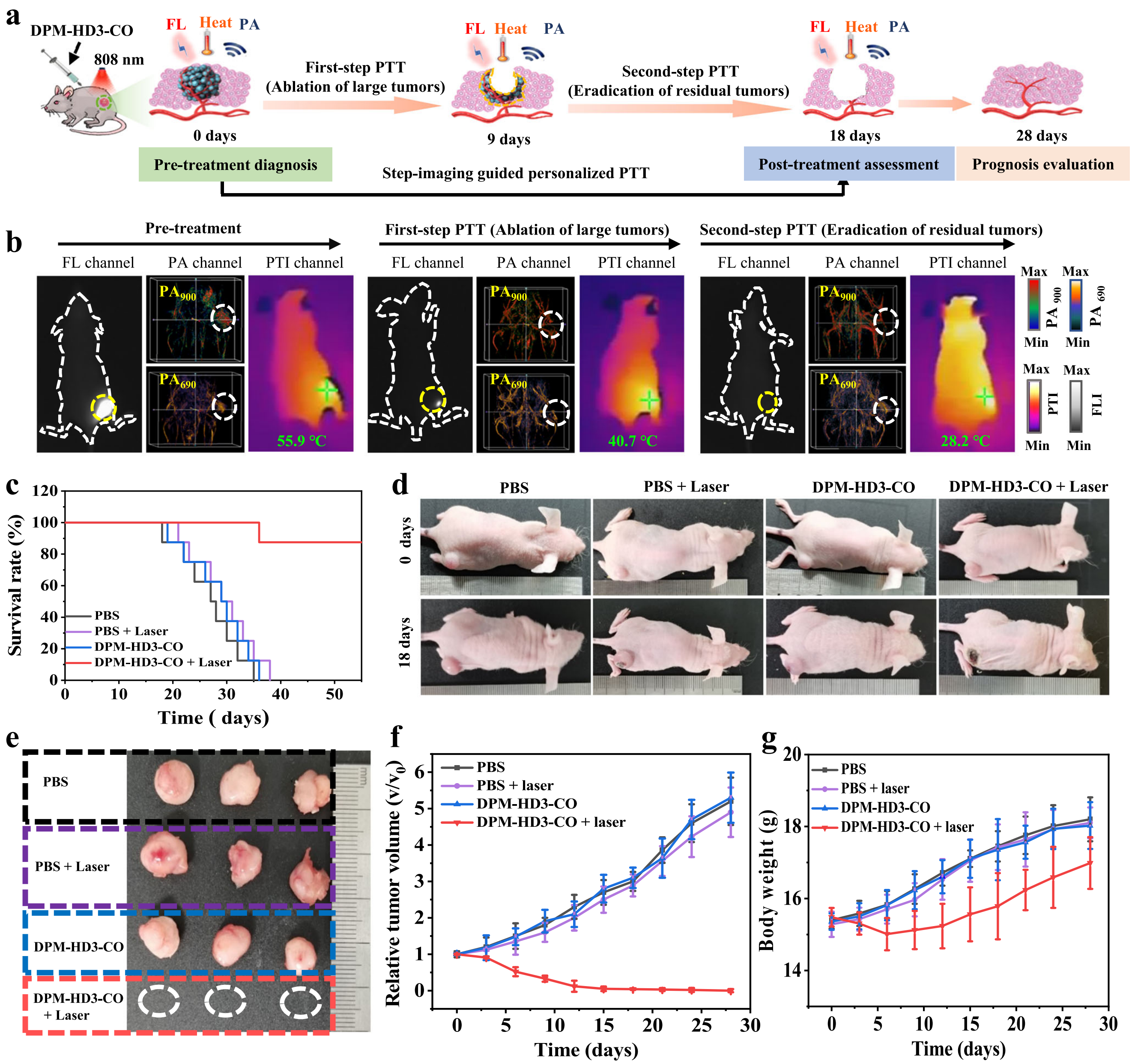

Fig. 6 | The multimodal theranostic agent for step-imaging guided personalized photothermal therapy. **a** Schematic illustration of **DPM-HD3-CO** for step-imaging guided personalized photothermal therapy in the tumor mice. **b** Representative NIR-II FLI/PAI/PTI of the Hepa1-6 tumor-bearing mice at pre-treatment, first-step PTT and second-step PTT. ($n = 8$ mice) FL imaging parameters: λ_{ex}: 808 nm, 880 nm long-pass filters. PA_{900} images excitation wavelength: 900 nm. PA_{690} images excitation wavelength: 690 nm. PTI images excitation wavelength: 808 nm. The meaning of the colors were indicated in the color bars: The gray and white represent FL channels. The red and green represent PA_{900} channel. The orange and purple represent PA_{690} channel. The yellow represent PTI channels. **c** Survival curves of the tumor-bearing mice after treatments with PBS, PBS + laser, **DPM-HD3-CO** (20 μM, 100 μL), and **DPM-HD3-CO** (20 μM, 100 μL) + laser. ($n = 8$ mice per group). **d** Representative photographs of the mice from the PBS, PBS + laser, **DPM-HD3-CO**, and **DPM-HD3-CO** + laser groups at 0 and 18 days. ($n = 8$ mice). **e** Representative photographs of the excised tumors at 18 days after treatments with PBS, PBS + laser, **DPM-HD3-CO** (20 μM, 100 μL), and **DPM-HD3-CO** (20 μM, 100 μL) + laser. ($n = 8$ mice). **f** The relationship between the relative tumor volume and treatment duration in the PBS, **DPM-HD3-CO** (20 μM, 100 μL), and **DPM-HD3-CO** (20 μM, 100 μL) + laser groups. ($n = 8$ mice). **g** The relationship between the mouse body weight and treatment duration in the PBS, **DPM-HD3-CO**, and **DPM-HD3-CO** + laser groups. Data are presented as the means ± s.d. ($n = 8$ mice, similar results were obtained.). Source data are provided as a Source Data file.

observed recurrence. The significant improvement in the survival rate for the **DPM-HD3-CO** + laser treatment group reflects the substantial advantage of the step-imaging guided therapy strategy. To further evaluate the efficacy of the step-imaging guided therapy strategy, the tumor volume changes were monitored following the photothermal therapy. The results of the treatment revealed that PBS and **DPM-HD3-CO** groups did not exhibit a significant therapeutic effect on the tumor (Fig. 6d, e). Conversely, the **DPM-HD3-CO** + laser group demonstrated significant inhibition effect of tumor growth, demonstrating that the photothermal properties of the probe could be specifically activated at the tumor site and possess excellent anti-tumor capability. The tumor size and weight of the mice were measured every 2 days during the treatment period to assess the treatment effect and side effects. As shown in Fig. 6f, the tumor growth remained stable in the absence of laser irradiation. However, when the probe was intratumorally injected and subjected to light therapy, the tumor growth was effectively suppressed, showing a trend towards complete elimination. In addition, the body weight of the mice in the probe + laser group slightly decreased at the beginning of treatment, but gradually increased with prolonged treatment duration, indicating the probe **DPM-HD3-CO** promising anti-tumor activity (Fig. 6g). The three control groups steadily gained the body weight during the treatment period, indicating the good biocompatibility of the probe. In addition, H&E histological analysis showed that only the tumor area showed significant damage after the photothermal treatment, while no lesions or injuries in the normal muscle tissues and major organs of heart, spleen, liver, lung, and kidney (Supplementary Figs. 91 and 92). This also further confirms that **DPM-HD3-CO** has low phototoxicity to the normal muscle tissues and does not produce significant side effects during the treatment. Consequently, the dual-property multimodal probe with CO activation developed in this study can be used as a companion diagnostic tool for the different treatment stages of cancer to achieve precise treatment of the individual tumors.

Discussion

In summary, we have proposed the concept of ACQ/AIE dual-properties multimodal luminescent materials, **DPMgens**. Significantly, **DPMgens** can simultaneously balance radiation and non-radiative transitions in both solution and solid states, exhibiting stable ACQ/AIE dual-properties multimodal luminescence. To demonstrate the advantages of **DPMgens**, we constructed a series of luminescent agents **DPM-HD1-3** with NIR-II FL, PA, and PT multimodal signals by manipulating the planar skeleton and twisted groups at the molecular and morphological levels. **DPM-HDs** can overcome the influence of heterogeneity accumulation effects, thus achieving high-fidelity multimodal luminescence in complex environments. Leveraging the unique ACQ/AIE dual-properties multimodal luminescent properties of **DPM-HDs**, we successfully customized an activatable dual-property multimodal therapeutic agent **DPM-HD3-CO** for step-imaging guided cancer heterogeneous therapy. The agent **DPM-HD3-CO** could overcome the interference caused by tumor heterogeneity and be utilized to reveal the relationship between CO levels and treatment response during the different stages of therapy, achieving accurate tumor detection and personalized therapy. The development of solid-liquid states multimodal probes not only provides an approach for the high-fidelity detection and accurate treatment of heterogeneous tumors, but also may open up the opportunity for monitoring other heterogeneous diseases and complex environments. More importantly, the development of **DPMgens** has addressed the impact of aggregation and dispersion on the optical performance of traditional single state dyes, thus heralding an era for dual-state multimodal chemical dyes. This breakthrough offers promising possibilities and forward-looking directions for research and applications in the areas such as biomedical imaging, environmental monitoring, chemical sensors, optoelectronic devices, and beyond.

Methods

Experimental animals

All animal experiments were approved by the Animal Experiment Ethics Committee of Guangxi University (Protocol Number: Gxu-2022-027). The 4-weeks-old female BALB/c-nu mice were purchased from the Laboratory Animal Center of the Guangxi Medical University (Nanning, China). Animals were kept in a controlled environment with a temperature of around 25 °C, humidity of 50 ± 10% and a light/dark period of 12 h. The maximum allowable tumor load was 2,000 mm^3, and the maximum tumor size was not exceeded in all trials.

Tracking the heterogeneous distribution of DPM-HD3-CO in cancer cells and tumor tissues

The Hepa1-6 cancer cells were seeded in confocal cell culture dishes at a density of 1×10^5 cells/dish for 12 h. To investigate the distribution of the probe **DPM-HD3-CO** in the cells, the Hepa1-6 cells were incubated with **DPM-HD3-CO** (20 μM, containing 10 μM $PdCl_2$) for 30 min. Then, the Hepa1-6 cells of the light exposure group were irradiated with 808 nm laser for 10 min. PBS group: the Hepa1-6 were incubated with PBS for 30 min. Probe group: the Hepa1-6 cells were incubated with 20 μM **DPM-HD3-CO** (containing 10 μM $PdCl_2$) for 30 min. Then, the laser confocal microscopy was used to image the Hepa1-6 cells treated with PBS, **DPM-HD3-CO**, or **DPM-HD3-CO** + Laser. The diameter of aggregates was analyzed using the Nano Measurer software. To investigate the potential impact of the probe **DPM-HD3-CO** heterogeneous distribution on the imaging performance, the Hepa1-6 cells from the PBS, probe **DPM-HD3-CO**, or probe **DPM-HD3-CO** + Laser treatment groups were digested with trypsin, then collected and centrifuged to obtain the cell pellets for FL and PA imaging. To study the distribution and therapeutic effect of the probe in the tumor/ tissue sections, 100 μL of **DPM-HD3-CO** (20 μM, containing 10 μM $PdCl_2$) was intratumorally injected into the tumor. For the specified light treatment group, the tumor region was irradiated with an 808 nm laser for 15 min. PBS (0.01 M, 100 μL) was intratumorally injected into the tumor as a control group. The tumor tissues from the PBS, probe **DPM-HD3-CO**, and probe **DPM-HD3-CO** + laser treatment groups (5 mice per group) were then excised, frozen sectioned, and subject to the confocal imaging. To evaluate the photothermal therapy effect of **DPM-HD3-CO**, the tumor tissue sections from the different treatment groups were stained with Calcein-AM or propidium iodide (live/dead cell staining reagents) for fluorescence imaging. To investigate the potential impact of the **DPM-HD3-CO** heterogeneous distribution in the tumor on the imaging performance, the tumors from the **DPM-HD3-CO** and **DPM-HD3-CO** treatment groups were excised for FL and PA imaging.

In vivo NIR-II FL, PA, and photothermal imaging

The Hepa1-6 tumor-bearing mice model was established by subcutaneously injecting a suspension of 1×10^6 Hepa1-6 cells into the back of the right hind leg. The Hepa1-6 tumor-bearing mice were intratumorally injected with 100 μL **DPM-HD3-CO** (20 μM, containing 10 μM $PdCl_2$). Then, at 0, 0.5, 6, 12, 24, 48 and 60 h post-injection, the mice were anesthetized using 2% isoflurane in oxygen and imaged through a commercial Series II 900/1700 imaging system with the long pass filter of 880 nm and quantitative analyses by Image J. Additionally, in vivo photoacoustic imaging was conducted using LOIS-3D photoacoustic imaging system (Tomo Wave Laboratories, USA) at designated time intervals following the intratumoral injection of 20 μM **DPM-HD3-CO** (100 μL, containing 10 μM $PdCl_2$). The infrared thermal images of mice were acquired using an IR camera during the irradiation of 808 nm laser (1 W/cm^2) for 10 min at 30 min after intratumorally injected with 20 μM **DPM-HD3-CO** (100 μL, containing 10 μM $PdCl_2$). The mouse intratumorally injected with PBS under the same irradiation condition were used as the control. To evaluate the metabolism of **DPM-HD3-CO** in vivo, we administered 100 μL of the probe **DPM-HD3-CO** (20 μM, 100 μL, containing 10 μM $PdCl_2$) via intratumoral injection to monitor its metabolism within the body. After 24 h post-injection, major organs (including the heart, liver, spleen, lungs, and kidneys) and tumor tissues were excised. Their surfaces were rinsed multiple times with saline for NIR-II fluorescence imaging.

In vivo photothermal therapy

The Hepa1-6 tumor-bearing mice were randomly divided into four groups (eight mice per group)): PBS group, PBS + laser group, **DPM-HD3-CO** group, and **DPM-HD3-CO** + laser group. For the first-step treatment, the mice were intratumorally injected with 100 μL of **DPM-HD3-CO** (20 μM, containing 10 μM $PdCl_2$). Subsequently, the tumor site was segmented irradiated (808 nm, 1 W/cm^2) for 5 min per session, repeated four times with a 20-min interval between each irradiation. On the 9th day following the completion of the first-step treatment, tumor therapeutic effects were assessed using NIR-II FL, PA, and photothermal imaging. For the second-step treatment, targeted therapy was administered based on the multimodal imaging results to completely eradicate residual microscopic tumors. The 20 μM **DPM-HD3-CO** (100 μL, containing 10 μM $PdCl_2$) were injected directly into the areas of residual tumor, followed by fractional irradiation of the residual tumor site with an 808 nm laser, three times per session, repeated twice with a 10-min interval between each session. On the 18th day following the completion of the treatment, tumor eradication and absence of recurrence were confirmed through NIR-II FL, PA, and photothermal imaging. To visualize the antitumor effect, the tumor-bearing mice were photographed on day 0 and 18. After a variety of treatments, the mouse body weight and tumor volume were recorded every 3 days during 28-day study duration. The tumor volume was measured by a vernier caliper and calculated as $V = a \times b^2/2$. (a: tumor length; b: tumor width). Relative tumor volume was calculated as $RTV = (V - V_0)/V_0$ (V_0 was the initial tumor volume). Relative body weight was calculated as $RBW = (W - W_0)/W_0$ (W_0 was the initial mouse body weight).

Statistics and reproducibility

Unless otherwise specified in figure legends, each experiment was repeated at least three times independently, and the results were similar. All images shown are representative results from biological replicates. Microsoft Excel 2016 and Origin 2018 was used to analyze the data in this study. The results are expressed as mean ± standard deviation (SD).

Reporting summary

Further information on research design is available in the Nature Portfolio Reporting Summary linked to this article.

Data availability

The data discussed in this study are presented in the manuscript, Supplementary information. All data are available from the corresponding author upon request. The Cartesian coordinates of optimized molecular geometry are provided in Supplementary Data 1-6. Source data are provided with this paper.

References

1. Schnermann, M. J. Organic dyes for deep bioimaging. *Nature* **551**, 176–177 (2017).
2. Sempionatto, J. R., Lasalde-Ramírez, J. A., Mahato, K., Wang, J. & Gao, W. Wearable chemical sensors for biomarker discovery in the omics era. *Nat. Rev. Chem.* **6**, 899–915 (2022).
3. Joo, W. J. et al. Metasurface-driven OLED displays beyond 10,000 pixels per inch. *Science* **370**, 459–463 (2020).
4. Hu, Y., Wang, J., Yan, C. & Cheng, P. The multifaceted potential applications of organic photovoltaics. *Nat. Rev. Mater* **7**, 836–838 (2022).
5. Turro, N. J. *In Modern Molecular Photochemistry*. (University Science Books, 1991).
6. Weiss, J. Fluorescence of organic molecules. *Nature* **152**, 176–178 (1943).
7. Friend, R. H. et al. Electroluminescence in conjugated polymers. *Nature* **397**, 121–128 (1999).
8. Mei, J., Leung, N. L. C., Kwok, R. T. K., Lam, J. W. Y. & Tang, B. Z. Aggregation-Induced Emission: Together We Shine, United We Soar! *Chem. Rev.* **115**, 11718–11940 (2015).
9. Luo, J. et al. Aggregation-induced emission of 1-methyl-1,2,3,4,5-pentaphenylsilole. *Chem. Commun* **18**, 1740–1741 (2001).
10. Wu, H. et al. Structural Engineering of Luminogens with High Emission Efficiency Both in Solution and in the Solid State. *Angew. Chemie - Int. Ed.* **58**, 11419–11423 (2019).
11. Rodríguez-Cortés, L. A., Navarro-Huerta, A. & Rodríguez-Molina, B. One molecule to light it all: The era of dual-state emission. *Matter* **4**, 2622–2624 (2021).
12. Yan, X., Cook, T. R., Wang, P., Huang, F. & Stang, P. J. Highly emissive platinum(II) metallacages. *Nat. Chem.* **7**, 342–348 (2015).
13. Shan, X. et al. Monomer and Excimer Emission in a Conformational and Stacking-Adaptable Molecular System. *Angew. Chemie - Int. Ed* **62**, e202215652 (2023).
14. Dufourt, J. et al. Imaging translation dynamics in live embryos reveals spatial heterogeneities. *Science* **372**, 840–844 (2021).
15. Stewart, P. S. & Franklin, M. J. Physiological heterogeneity in biofilms. *Nat. Rev. Microbiol.* **6**, 199–210 (2008).
16. Goossens, P. et al. Integrating multiplex immunofluorescent and mass spectrometry imaging to map myeloid heterogeneity in its metabolic and cellular context. *Cell Metab* **34**, 1214–1225 (2022).
17. Zhanghao, K. et al. High-dimensional super-resolution imaging reveals heterogeneity and dynamics of subcellular lipid membranes. *Nat. Commun* **11**, 1–10 (2020).
18. Galeano Niño, J. L. et al. Effect of the intratumoral microbiota on spatial and cellular heterogeneity in cancer. *Nature* **611**, 810–817 (2022).
19. Buzzetti, R., Zampetti, S. & Maddaloni, E. Adult-onset autoimmune diabetes: current knowledge and implications for management. *Nat. Rev. Endocrinol* **13**, 674–686 (2017).
20. Bedard, P. L., Hansen, A. R., Ratain, M. J. & Siu, L. L. Tumour heterogeneity in the clinic. *Nature* **501**, 355–364 (2013).
21. Li, S. et al. Distinct evolution and dynamics of epigenetic and genetic heterogeneity in acute myeloid leukemia. *Nat. Med.* **22**, 792–799 (2016).
22. Wang, J., Li, Y. & Nie, G. Multifunctional biomolecule nanostructures for cancer therapy. *Nat. Rev. Mater.* **6**, 766–783 (2021).
23. Brindle, K. New approaches for imaging tumour responses to treatment. *Nat. Rev. Cancer* **8**, 94–107 (2008).
24. Park, S. M., Aalipour, A., Vermesh, O., Yu, J. H. & Gambhir, S. S. Towards clinically translatable in vivo nanodiagnostics. *Nat. Rev. Mater.* **2**, 17014 (2017).
25. Hong, G., Antaris, A. L. & Dai, H. Near-infrared fluorophores for biomedical imaging. *Nat. Biomed. Eng.* **1**, 0010 (2017).
26. Salgado, R. et al. Steps forward for cancer precision medicine. *Nat. Rev. Drug Discov* **17**, 1–2 (2018).
27. Balzarotti, F. et al. Nanometer resolution imaging and tracking of fluorescent molecules with minimal photon fluxes. *Science* **355**, 606–612 (2017).
28. Dragulescu-Andrasi, A., Kothapalli, S. R., Tikhomirov, G. A., Rao, J. & Gambhir, S. S. Activatable oligomerizable imaging agents for photoacoustic imaging of furin-like activity in living subjects. *J. Am. Chem. Soc.* **135**, 11015–11022 (2013).
29. Jiménez-Sánchez, A. et al. Heterogeneous Tumor-Immune Microenvironments among Differentially Growing Metastases in an Ovarian Cancer Patient. *Cell* **170**, 927–938.e20 (2017).
30. Bianchini, G., Balko, J. M., Mayer, I. A., Sanders, M. E. & Gianni, L. Triple-negative breast cancer: challenges and opportunities of a heterogeneous disease. *Nat. Rev. Clin. Oncol* **13**, 674–690 (2016).
31. Ding, Q. et al. Diverse interactions between AIEgens and biomolecules/organisms: Advancing from strategic design to precision theranostics. *Chem.* **10**, 2031–2073 (2024).
32. Schmidt, E. L. et al. Near-infrared II fluorescence imaging. *Nat. Rev. Methods Prim.* **4**, 23 (2024).
33. Li, J. et al. Aggregation-induced emission fluorophores towards the second near-infrared optical windows with suppressed imaging background. *Coord. Chem. Rev.* **472**, 214792 (2022).
34. Brøndsted, F. et al. Acoustic Loudness Factor: An Experimental Parameter for Benchmarking Small Molecule Photoacoustic Probes. ChemRxiv. *ChemRxiv* (2024).
35. Xue, K. et al. A Sensitive and Reliable Organic Fluorescent Nanothermometer for Noninvasive Temperature Sensing. *J. Am. Chem. Soc.* **143**, 14147–14157 (2021).

36. Allouche, A. Software News and Updates Gabedit — A Graphical User Interface for Computational Chemistry Softwares. *J. Comput. Chem.* **32**, 174–182 (2012).
37. Yankeelov, T. E., Abramson, R. G. & Quarles, C. C. Quantitative multimodality imaging in cancer research and therapy. *Nat. Rev. Clin. Oncol.* **11**, 670–680 (2014).
38. Boehm, K. M., Khosravi, P., Vanguri, R., Gao, J. & Shah, S. P. Harnessing multimodal data integration to advance precision oncology. *Nat. Rev. Cancer* **22**, 114–126 (2022).
39. Boehm, K. M. et al. Multimodal data integration using machine learning improves risk stratification of high-grade serous ovarian cancer. *Nat. Cancer* **3**, 723–733 (2022).
40. Gow, A. J. & Stamler, J. S. Reactions between nitric oxide and haemoglobin under physiological conditions. *Nature* **391**, 169–173 (1998).
41. Motterlini, R. & Otterbein, L. E. The therapeutic potential of carbon monoxide. *Nat. Rev. Drug Discov* **9**, 728–743 (2010).
42. Klemz, R. et al. Reciprocal regulation of carbon monoxide metabolism and the circadian clock. *Nat. Struct. Mol. Biol.* **24**, 15–22 (2017).
43. Feng, W., Liu, D., Feng, S. & Feng, G. Readily Available Fluorescent Probe for Carbon Monoxide Imaging in Living Cells. *Anal. Chem.* **88**, 10648–10653 (2016).
44. Song, F., Garner, A. L. & Koide, K. A highly sensitive fluorescent sensor for palladium based on the allylic oxidative insertion mechanism. *J. Am. Chem. Soc.* **129**, 12354–12355 (2007).
45. Lazarus, L. S., Benninghoff, A. D. & Berreau, L. M. Development of Triggerable, Trackable, and Targetable Carbon Monoxide Releasing Molecules. *Acc. Chem. Res.* **53**, 2273–2285 (2020).
46. Fujita, K. et al. Intracellular CO release from composite of ferritin and ruthenium carbonyl complexes. *J. Am. Chem. Soc.* **136**, 16902–16908 (2014).
47. Chau, L. Y. Heme oxygenase-1: Emerging target of cancer therapy. *J. Biomed. Sci.* **22**, 1–7 (2015).
48. Marte, B. Tumour heterogeneity. *Nature* **501**, 327 (2013).

Acknowledgements

This work was financially supported by National Natural Science Foundation of China (22277014, W. Lin, and 22077048, W. Lin), Guangxi Natural Science Foundation (2021GXNSFDA075003, W. Lin, AD21220061, W. Lin), and the startup fund of Guangxi University (A3040051003, W. Lin).

Author contributions

Weiying Lin (W. Lin) and Wenxiu Li (W. Li) conceived project and designed experiments; W. Li, Sixin Ai (S. A.) and Huayong Zhu (H. Z.) performed research; W. Li, S. A. and H. Z. analyzed the data; W. Li and W. Lin wrote the original draft and revised the manuscript. W. Lin contributed to project supervision and funding acquisition. All authors have read and approved the final version of the manuscript.

Competing interests

The authors declare no competing interests.

Additional information

Supplementary information The online version contains supplementary material available at https://doi.org/10.1038/s41467-025-57673-1.

Correspondence and requests for materials should be addressed to Weiying Lin.

Peer review information *Nature Communications* thanks Hao Wang, who co-reviewed with Hongwei Wu and the other, anonymous, reviewer(s) for their contribution to the peer review of this work. A peer review file is available.